Thermal Imaging of Nanostructures by Quantitative Optical Phase Analysis

Guillaume Baffou,[†,*] Pierre Bon,[†,‡] Julien Savatier,[†] Julien Polleux,[§,#] Min Zhu,[§] Marine Merlin,[†] Hervé Rigneault,[†] and Serge Monneret[†]

[†]Institut Fresnel, UMR CNRS 7249, Domaine Universitaire Saint-Jérôme, 13397 Marseille, France, [‡]PHASICS SA, Campus de l'Ecole Polytechnique, 91128 Palaiseau, France, [§]Department of Molecular Medicine, Max Planck Institute of Biochemistry, 82152 Martinsried, Germany, and [#]Department of New Materials and Biosystems, Max Planck Institute for Intelligent Systems, 70569 Stuttgart, Germany

ABSTRACT

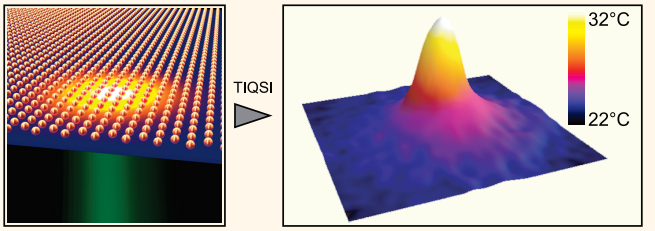

We introduce an optical microscopy technique aimed at characterizing the heat generation arising from nanostructures, in a comprehensive and quantitative manner. Namely, the technique permits (i) mapping the temperature distribution around the source of heat, (ii) mapping the heat power density delivered by the source, and (iii) retrieving the absolute absorption cross section of light-absorbing structures. The technique is based on the measure of the thermal-induced refractive index variation of the medium surrounding the source of heat. The measurement is achieved using an association of a regular CCD camera along with a modified Hartmann diffraction grating. Such a simple association makes this technique straightforward to implement on any conventional microscope with its native broadband illumination conditions. We illustrate this technique on gold nanoparticles illuminated at their plasmonic resonance. The spatial resolution of this technique is diffraction limited, and temperature variations weaker than 1 K can be detected.

KEYWORDS: microscopy · thermodynamics · phase imaging · plasmonics · gold nanoparticles

Probing temperature at the nanoscale is fundamentally a complicated task mainly because heat has a nonpropagative nature, unlike light. Yet, the ability to investigate thermal-induced phenomena on the nanoscale would help in the development of unprecedented applications in many active current areas of research,[1] namely, photothermal cancer therapy,[2,3] drug release,[4] nanosurgery,[5] opto-acoustic imaging,[6,7] nanochemistry,[8,9] microfluidics,[10] magnetic recording[11] and thermonics.[12] Twenty years ago, as a temperature microscopy technique, the use of a sharp hybrid tip as a nanothermocouple was proposed.[13,14] Even though such an approach achieved a spatial resolution of 50 nm, it appeared to be very invasive due to the proximity of the tip to the sample. More recently, several thermal microscopy techniques have been developed that are much less invasive since they are based on far-field optical measurements. These optical techniques rely either on fluorescence intensity,[15,16] fluorescence polarization anisotropy,[17,18] fluorescence spectroscopy,[19−21] Raman spectroscopy,[22] infrared spectroscopy,[23] or X-ray spectroscopy[24] measurements. However, all these techniques suffer from drawbacks that make them suited only for particular cases. Namely, they suffer from a slow read-out rate,[19−22] a low resolution,[23] a lack of reliability,[15,16] a poor temperature sensitivity,[22] or the necessity to modify (tag) the medium with fluorescent molecules or nanocrystals.[15−21]

In this paper, we propose a thermal microscopy technique sensitive to the thermal-induced variation of the refractive index of the medium of interest. This optical technique circumvents the limitations of all the previous techniques mentioned above and is straightforward to implement on any conventional optical microscope. We explain how it leads to a quantitative real-time retrieval of the distributions of both the temperature and the source of heat with a submicrometric resolution. The theory and the retrieval algorithms are detailed. We chose to illustrate the capabilities of this technique on gold nanoparticles (NPs), which act as ideal nanosources of heat when illuminated at their plasmonic resonance frequency. Moreover, we show how a quantitative measurement of the actual absorption cross section can be achieved, whatever the nature of the absorbing structure. We chose to name this technique TIQSI for thermal imaging using quadriwave shearing interferometry.

* Address correspondence to guillaume.baffou@Fresnel.fr.

Received for review December 6, 2011 and accepted February 3, 2012.

Published online February 03, 2012
10.1021/nn2047586

RESULTS AND DISCUSSION

We consider in this work a two-dimensional distribution of absorbers (gold nanoparticles) distributed at the interface between a solid (glass substrate) and a liquid environment (like water). When the absorbers are illuminated, heat is generated and a temperature steady state profile appears over a time scale that depends on the spatial extension of the source of heat (typically below 10 μs for structures smaller than 1 μm, in water[25]). This temperature increase is responsible for a variation of the refractive index of the surrounding liquid over a typical length much larger than the size of the particle itself. This effect has been recently exploited independently by the groups of Lounis and Orrit as a localization technique of NPs or single molecules.[26−29] NPs and molecules of interest in these works were nonluminescent and far too small to scatter any incident light, making them invisible using any conventional optical technique. To circumvent this limitation, the idea developed in these groups was to exploit the light absorption capabilities of the nano-objects to thermally induce an extended variation of the refractive index of the surroundings, much easier to detect than the nano-objects themselves. However, this localization technique is based on the modulation of the heating laser to achieve an heterodyne detection. For this reason, it cannot be used to measure any *steady-state* temperature distribution. Moreover, this technique remains slow and requires a complex experimental configuration comprising an acousto-optical modulator and a heterodyne detection.

Recently, our group has developed an optical phase microscopy technique capable of mapping quantitatively the optical path difference (OPD) through a refractive object in real time with a sensitivity of ~1 nm.[30] This technique was illustrated by imaging microscopic dielectric beads and living organisms. The experimental approach is based on the use of a quadriwave lateral shearing interferometer as a wavefront analyzer (WFA) (see Supporting Information for more details). Basically, it consists of a modified Hartmann grating (MHG) associated with a regular CCD camera. The device, named Sid4Bio, was purchased from Phasics SA.[31] The interferogram produced by the MHG and recorded by the CCD camera can be processed in real time to retrieve the OPD. Interestingly, this interferometric technique is achromatic and can be mounted on any conventional white-light transmission microscope. In the present work, we demonstrate how this experimental approach can be the basis of an efficient and easy-to-implement thermal imaging technique. The experimental setup is detailed in Figure 1. All the samples we used consist of a sandwich structure where a water layer of thickness h is limited by two glass coverslips in the z direction. The gold nanoparticles

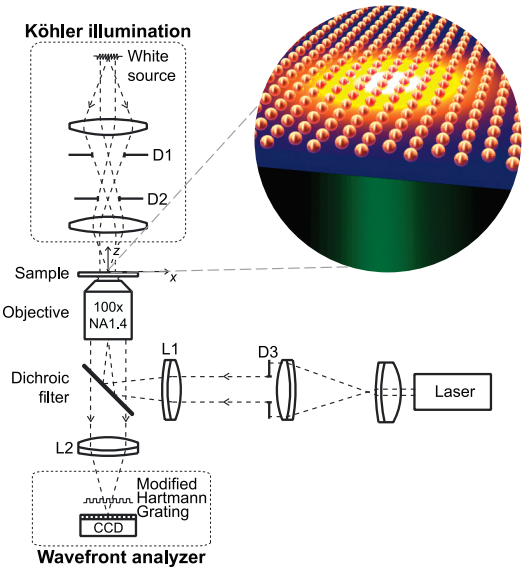

Figure 1. Schematic of the experimental setup. The sample is illuminated using a Köhler configuration with a reduced numerical aperture (D2) to increase the spatial coherence of the light. A laser is used to excite the gold structures at their plasmonic resonance and heat them (either at 532 or 808 nm, depending of the sample). It is focused at the objective entrance pupil by L1 to perform a wide field illumination. A diaphragm D3 is used to control the beam diameter and to achieve a uniform illumination at the sample location. This diaphragm is optically conjugated with the sample by the objective/L1 association The sample is imaged onto a CCD camera by L2 through a modified Hartmann grating. This creates an interferogram on the CCD that is processed to retrieve the optical path difference generated by the thermal-induced refractive index variation.

acting as nanosources of heat are lying on the bottom coverslip.

When experiencing a temperature variation $\delta T(\mathbf{r}) = T(\mathbf{r}) - T_\infty$, a given medium undergoes a variation $\delta n(\mathbf{r})$ of its refractive index. This variation is usually described by a Taylor development of the Nth order:[32]

$$\delta n = \sum_{j=1}^{N} \beta_j \delta T^j \qquad (1)$$

where β_j are empirical parameters (see Supporting Information or ref 32 for values). For the sake of simplicity, we shall consider in this theoretical part only the first (linear) term of this Taylor series: $\delta n = \beta_1 \delta T$. In water, this assumption is valid if the temperature increase over the ambient temperature does not exceed ~20 °C.[32] It makes the equations linear and simplifies the algorithm used to retrieve the temperature profile. When higher temperature increases are considered, a nonlinear iterative numerical procedure is required. The approach is more complex but still simple to implement as detailed in Supporting Information.

To begin with, let us consider a *point-like* source of heat located at the solid−liquid planar interface at $(x,y,z) = (0,0,0)$. In the surrounding liquid, the temperature

distribution is governed by the Poisson equation:

$$\kappa \nabla^2 T(\mathbf{r}) = P_0 \delta(\mathbf{r}) \quad (2)$$

where κ is the thermal conductivity of the surrounding liquid (0.6 W/m/K for water), $T(\mathbf{r})$ the temperature and P_0 the power absorbed (*i.e.*, delivered) by the point-like source of heat. In spherical coordinates, the solution reads

$$T(r) = T_\infty + \frac{P_0}{4\pi\kappa r} = T_\infty + \frac{\bar{P}_0}{r} \quad (3)$$

$$T(r) = T_\infty + \bar{P}_0 G_T(r) \quad (4)$$

where T_∞ is the ambient temperature, $\bar{P}_0 = P_0/(4\pi\kappa)$ is the normalized power, and $G_T(r) = 1/r$ the standard Green's function associated to the Poisson equation.

Experimentally, we use the WFA to measure two phase images of a given area: One reference image acquired (once far all) without heating and one image under heating. The subtraction of these two images provides a measure of the spatial distribution of the optical path difference $\delta\ell(x, y)$ through the liquid layer specifically due to thermal-induced variation of the refractive index distribution $\delta n(x,y,z)$. It can be written as

$$\delta\ell(x, y) = \int_0^h \delta n(\mathbf{r})\, dz = \int_0^h \beta_1 \delta T(\mathbf{r})\, dz \quad (5)$$

According to eq 3, the profile of the temperature variation δT reads in radial coordinates (ρ,z):

$$\delta T(\rho, z) = \frac{\bar{P}_0}{\sqrt{\rho^2 + z^2}} \quad (6)$$

Using eqs 5 and 6 and after integration, the OPD reads

$$\delta\ell(\rho) = \bar{P}_0 \beta_1 \ln(h/\rho + \sqrt{1 + (h/\rho)^2}) \quad (7)$$

$$\delta\ell(\rho) = \bar{P}_0 \beta_1 \sinh^{-1}(h/\rho) = \bar{P}_0 G_\ell(\rho) \quad (8)$$

where $G_\ell(\rho) = \beta_1 \sinh^{-1}(h/\rho)$ stands for the Green's function for the phase distribution, since the source of heat is a Dirac distribution. By eliminating the radial coordinate ρ in eqs 6 and 7, one ends up with a bijective relation between the optical phase difference and the temperature increase at $z = 0$:

$$\delta T(\rho, 0) = \frac{\bar{P}_0}{h} \sinh\left(\frac{\delta\ell(\rho)}{\bar{P}_0 \beta_1}\right) \quad (9)$$

Note that this formula is only valid for a point-like source of heat, since it was derived using eq 6. In the most general case (extended and nonuniform source of heat), such a bijective relation does not exist between the OPD and the temperature and an deconvolution procedure is required, which we shall detail now.

Consider now an extended nonuniform source of heat characterized by a delivered heat power density (HPD) $p(x,y) = 4\pi\kappa\bar{p}(x,y)$. The subsequent OPD and temperature distributions can be expressed as convolutions with the associated Green's functions:

$$\delta\ell(x, y) = [\bar{p} \otimes G_\ell](x, y) \quad (10)$$

$$\delta T(x, y) = [\bar{p} \otimes G_T](x, y) \quad (11)$$

which turns into simple multiplications in the Fourier domain:

$$\widetilde{\delta\ell}(\mathbf{k}) = \widetilde{\bar{p}}(\mathbf{k}) \tilde{G}_\ell(\mathbf{k}) \quad (12)$$

$$\widetilde{\delta T}(\mathbf{k}) = \widetilde{\bar{p}}(\mathbf{k}) \tilde{G}_T(\mathbf{k}) \quad (13)$$

where $\tilde{f}$ stands for the Fourier transform of f. From the experimental phase image $\delta\ell(x, y)$, the heat source distribution $\bar{p}(x,y)$ can be simply retrieved using eq 12: $\widetilde{\bar{p}}(\mathbf{k}) = \widetilde{\delta\ell}(\mathbf{k})/\tilde{G}_\ell(\mathbf{k})$ followed by an inverse Fourier transform. However, such a basic approach is likely to cause divergence problems in the case of low signal-to-noise ratio in the OPD images. This standard deconvolution issue is well-known, and different approaches have been proposed in the literature. Among them, one of the simplest is the Tikhonov regularization method,[33] which we used here. Its principle is detailed in Supporting Information. Then, the temperature distribution $T(x,y)$ is retrieved using eq 13 followed by an inverse Fourier transform.

The spatial resolution of the TIQSI technique is given by λ/NA (since the illumination is spatially coherent) where λ is the characteristic wavelength of the Köhler illumination and NA is the numerical aperture of the objective. Our set of measurements corresponds to λ = 650 nm and NA = 1.4, which leads to a theoretical spatial resolution of around 450 nm. The frame rate of our CCD camera is 10 Hz (100 ms per image). We usually average a series of 10 to 30 frames to improve the signal-to-noise ratio. Hence, one usually needs a few seconds per image. This is much faster than most of the other thermal microscopy techniques, which need a few minutes or even a few hours to record an image. This readout rate is not a fundamental limitation of the TIQSI technique, and it could be improved with a faster and better cooled CCD camera.

We shall first present and discuss experimental results obtained on a point-like source of heat, that is, a gold disk, 300 nm in diameter and 40 nm thick illuminated by a laser beam at λ_0 = 808 nm (Figure 2a). Figure 2b displays the raw image of the OPD measured by the WFA. From this image, we have applied the Tikhonov algorithm to retrieve the actual HPD and temperature distributions, as displayed in Figure 2c,d. Interestingly, the temperature extension (Figure 2d) is much narrower than the extension of the OPD distribution. This observation is consistent with the $-\ln(\rho)$ decrease of the OPD Green's function (eq 7), compared to the much steeper $1/\rho$ decrease of the temperature Green's function (eq 4). In this measurement, 30 frames

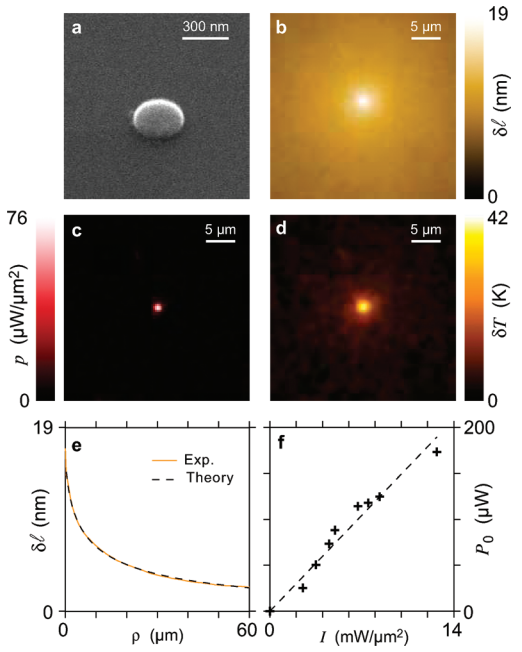

Figure 2. (a) Scanning electronic microscope (SEM) image of the gold structure under study. This structure was illuminated at a wavelength λ_0 = 808 nm. (b) Raw image of $\delta(x,y)$, I = 12.8 mW/μm^2. (c) Heat power density $p(x,y)$ processed from image b using the NL algorithm. (d) Temperature distribution $\delta T(x,y)$ processed from image c using eq 11. (e) Measured radial profile of the OPD distribution in image b (solid line), fitted using eq 9 (dashed line). (f) Delivered power P_0, as function of the laser irradiance, measured by fitting the OPD radial profile using eq 9 with P_0 and h as the unknown parameters.

of 100 ms were averaged. The standard deviation of the noise in the raw OPD image (Figure 2b) is 0.15 nm and in the temperature image (Figure 2d), 1.1 K.

In experimental optics, determining the actual absorption cross section (ACS) of a unique absorber is not straightforward mainly because the absorption process is precisely not associated with any light reemission that could contain information and be detected in the far-field (unlike extinction or scattering cross sections measurements). Optical techniques to measure ACS have been proposed recently.[34,35] However, all of them suffer from at least one of these drawbacks: (i) They consist in fact in measuring extinction instead of absorption. This assimilation is valid only for small particles, for instance, when scattering is negligible (extinction = absorption + scattering). (ii) They do perform absorption spectroscopy, but they do not yield a quantitative measurement of the cross section. In this second case, a quantitative ACS can be eventually estimated indirectly by comparing the photothermal signal with the one obtained on a reference absorber with a supposedly known ACS.[29] Our approach circumvents these two limitations at the same time: It allows the acquisition of a direct quantitative measurement of the actual absorption cross section σ_{abs} without any assumption and independently of the nature of the absorber. One just needs to estimate the absorbed power P_0 and then calculate $\sigma_{abs} = P_0/I$ where I is the irradiance of the laser beam (power per unit area). There are two possibilities to estimate P_0. The first one consists in fitting the radial profile of the OPD image (as shown in Figure 2e) using equation 7 with P_0 (and eventually h) as the unknown parameter. This first approach gives in the case of Figure 2: σ_{abs} = 14930 $\pm$ 530 nm^2. The second approach consists in estimating P_0 by a spatial integration of the HPD image (Figure 2c). It naturally yields a very similar result: σ_{abs} = 15300 $\pm$ 600 nm^2. Calculations using the Green's dyadic tensor method[18] on a gold disk, 288 nm in diameter, 39 nm thick, discretized using 2066 cells and illuminated at λ = 808 nm, led to σ_{abs} = 17200 nm^2, which is the good order of magnitude. The difference of 14% with the experimental measurement can be mainly explained by the fact that the real structure is not a perfect disk. The accuracy of the measurement can be optimized by acquiring a set of images at different irradiances, as illustrated in Figure 2f. The first approach is handy since it does not require the computation of the HPD distribution, while the second approach is more general and applies even for extended (not point-like) sources of heat. Note that one does not need to optically resolve the NP to measure its ACS. Indeed, the ACS retrieval procedure is based on the fit of the logarithmic OPD profile around the particle that extends to infinity, even for nanometric/point-like particles (see Figure 2a–c).

We shall now present experimental results that address the situation of an extended distribution of heat sources. In Figure 3, experiments have been carried out on an array of quasi-hexagonally organized NPs. The sample has been done by block-copolymer lithography.[36] It consists of spherical gold NPs, d = 30 $\pm$ 3 nm in diameter and separated by p = 100 $\pm$ 10 nm. The NP interdistance is small enough compared to the resolution of the microscope to consider the HPD as a continuous physical quantity. The heat is generated by a laser beam at λ_0 = 532 nm, close to the resonance wavelength of the gold particles. In the first case, the NP array covers the whole sample (Figure 3a) and the laser illuminates uniformly a circular area of diameter 8.0 μm. In the second case, NP distributions form cross-like structures (Figure 3f). One of them is uniformly illuminated by the heating laser. From the optical path difference measured by the WFA (Figure 3b–g) the distribution of the HPD is computed using the Tikhonov inversion algorithm. As expected, the heat source distributions (Figure 3c–h) are well delimited while the temperature distributions tend to spread out (Figure 3d–i). To verify the consistency of the temperature distribution, we performed numerical simulation of the temperature profile in Figure 3d using the Green's function formalism[25] (Figure 3e). The input

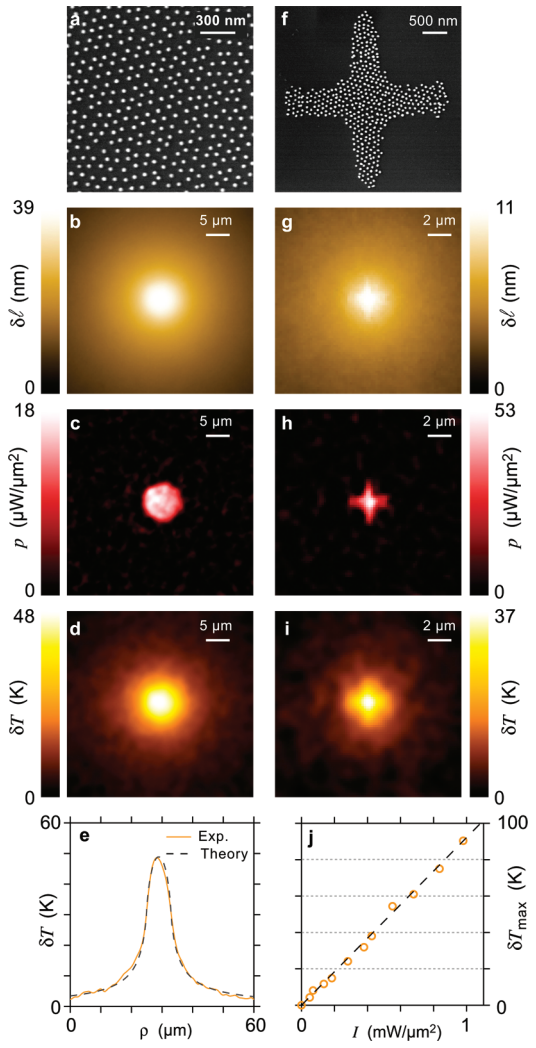

Figure 3. (a) SEM image displaying a quasi-hexagonally ordered array of gold nanoparticles; (b) raw image of the measured optical path difference. Heating is performed by a circular beam of diameter $D = 8.0\ \mu$m and uniform irradiance 105 μW/μm^2 at $\lambda = 532$ nm; (c) processed heat power density; (d) processed temperature increase; (e) radial profile of the temperature distribution; (f) optical image of the micropatterned array of gold nanodots. This whole structure is illuminated by a uniform beam of irradiance 250 μW/μm^2; (g) raw image of the measured optical path difference; (h) heat source density; (i) temperature increase; (j) maximum temperature of the microstructure as function of the laser irradiance.

parameters regarding the geometry and the illumination conditions were $I = 105\ \mu$W/μm^2, $D = 8.0\ \mu$m, $p = 105$ nm, $d = 28$ nm. The only variable parameters were d and p which remain very close to the measured values on the SEM image. The matching is very good as observed in Figure 3e, which reinforces the validity of our postprocessing numerical model. A last result that we wish to share is presented in Figure 3j. It shows that, as expected, the temperature increase is proportional to the laser irradiance, even over a wide range of temperature. The nonlinearities of the problem are thus well taken into account in our numerical procedure (see Supporting Information).

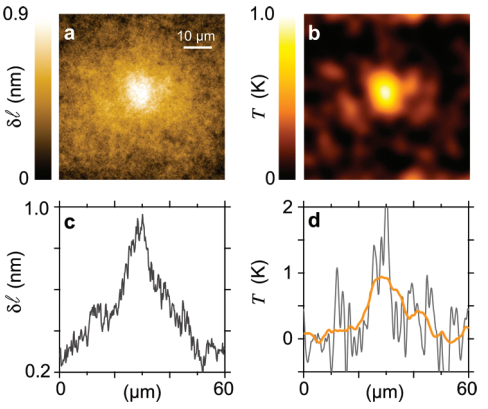

Figure 4. (a) Raw thermal-induced OPD image obtained on a quasi-hexagonally ordered array of gold nanoparticles (see Figure 3a). (b) Processed temperature distribution (smoothed using a 10-pixel Gaussian function). (c) Cross section of image a. (d) Cross section of the raw image (b) without smoothing (dash line) and with smoothing (solid line).

In this last paragraph, we wish to discuss the temperature sensitivity that the TIQSI method can achieve. Figure 4 presents a measurement performed on an extended quasi-hexagonal array of nanodots. The structure is illuminated by a uniform circular beam of diameter 11 μm and power $P = 0.35$ mW. Such a low irradiance ($I = 3.7\ \mu$W/μm^2) led to a fairly noisy OPD image (Figure 4a) due to a weak temperature increase. Processing of the OPD image led to a temperature image presented in Figure 4b and revealed that the temperature increase was about 1 K. One can see that such a temperature increase is perfectly visible on the OPD image, even though it leads to a very noisy temperature image. The standard deviation of the noise in the OPD image (Figure 4a) is 0.044 nm and in the temperature image (Figure 4b), 0.36 K. The higher noise level in the temperature image compared with the OPD image is inherent to the deconvolution procedure, and mostly features low frequencies. Below a temperature increase of 1 K, it is hard to obtain a well-defined temperature map. However, since most of the noise observed on the interferogram recorded by the CCD image is due to dark current, it could be possible to increase the signal-to-noise ratio and reach even better temperature sensitivity by increasing the number of accumulated frames, or by using a better cooled CCD camera. In this work, we chose a water environment in order to match the usual conditions of the potential applications, but another way to improve the temperature sensitivity could be to use a liquid medium featuring a higher $\beta 1$ value like alcohols or alkanes. Note that no physical limitation exists on the temperature accuracy, unlike the spatial resolution that is bound to remain diffraction-limited.

CONCLUSION

We introduced a thermal microscopy technique sensitive to thermal-induced refractive index variation.

The measurement is achieved using a simple experimental configuration consisting of a Hartmann diffraction grating attached to a CCD camera. This technique, which we named TIQSI, cumulates many valuable advantages compared with previous thermal imaging techniques: (i) It is fast. According to the CCD frame rate, it takes around one second to acquire an acceptable image in most cases. (ii) No scanning is required. It is a one-shot measurement of a 2D image. (iii) It has a diffraction limited resolution (less than 500 nm). (iv) No modification of the sample is required, like using fluorescent markers. It works whatever the sample as far as there is a liquid environment. (v) No need to use sophisticated devices such as heterodyne detection, acousto-optic modulator, and spectrometer, etc., like previous thermal imaging techniques. All the thermal measurements can be performed by plugging in the CCD/grating device on a conventional optical microscope, just like a regular CCD camera. (vi) The TIQSI technique features an unprecedented versatility since it can quantitatively measure temperature, heat source density, and absorption cross sections of nanoparticles and nanostructures. We chose to illustrate the abilities of the technique on gold NPs, which stand for ideal nanosources of heat. However, we wish to emphasize that the method is not restricted to metal NPs and can be extended to any 2D-distribution of heat sources, independent of their nature. Moreover, this technique is straightforward to implement on any conventional microscope. For these reasons, pending important applications are envisioned not only in plasmonics but also in areas such as nanoelectronics, microfluidics, or cell biology.

METHODS

Fabrication of the Quasi-hexagonal Arrays of Gold Nanodots. In a typical synthesis, polystyrene(1056)-block-poly(2-vinylpyridine)-(495) (PS1056-*b*-P2VP495) from Polymer Source Inc. was dissolved at room temperature in anhydrous toluene (Sigma-Aldrich) with a concentration of 5 mg/mL and stirred for 2 days. The quantity of gold precursor was calculated relative to the number of P2VP units with a loading parameter equal to 0.5, that is, 1 molecule of $HAuCl_4$ for 2 P2VP monomers. Hydrogen tetrachloroaurate (III) trihydrate ($HAuCl_4 \cdot 3H_2O$, Sigma-Aldrich) was added to the dBCP solution and stirred for 2 days in a sealed glass vessel. Glass coverslips (Carl Roth) were cleaned in a piranha solution for at least 5 h and were extensively rinsed with Milli-Q water and dried under a stream of nitrogen. Micellar monolayers were prepared by dip-coating a glass coverslip into the previously prepared solutions with a constant velocity equal to 24 mm/min. To remove the organic template and to form inorganic nanoparticles, the dip-coated glass slides were exposed to oxygen plasma (150 W, 0.15 mbar, 45 min, PVA TEPLA 100 Plasma System). In the case of the micropatterned arrays of gold nanodots, a 1-μm thick layer of AR-P5350 photoresist (Allresist GmbH) was spin-coated onto the arrays. Illumination was performed under a maskaligner (Suss Microtec GmbH) with a dose of 175 mJ/cm^2 from a HBO 350 mercury lamp, and the microstructures were developed according to the manufacturer's instructions.[36] The enlargement of gold nanodots was performed in an aqueous solution containing hydroxylamine (0.02 mM) and $HAuCl_4$ (0.1 wt %) for 10 min. Scanning electron measurements were performed with a Dual BeamTM (FIB/SEM) instrument (Quanta 3D FEG, FEI, Hillsboro).

Conflict of Interest: The authors declare the following competing financial interest: PB was a PhD student from September 2008 to December 2011 with a financial support that came partly from the Phasics company.

Acknowledgment. We acknowledge fruitful discussions with Philippe Réfrégier. We thank the Institute of Photonic Sciences (ICFO) for providing the lithographic sample (Figure 2a) . We acknowledge financial support from the region Provence-Alpes-Cote d'Azur, the Fonds Unique Interministériel (QuITO project), the Centre National de la Recherche Scientifique, the 7th Framework Program of the European Community (FP7) through the Marie Curie Action for career development (IEF-"Multi-PGNAs") and the Max Planck Society.

Supporting Information Available: Additional figures and calculations as described in the text. This material is available free of charge *via* the Internet at http://pubs.acs.org.

REFERENCES AND NOTES

1. Govorov, A. O.; Richardson, H. H. Generating Heat with Metal Nanoparticles. *Nano Today* **2007**, *2*, 30.
2. Lal, S.; Clare, S. E.; Halas, N. J. Nanoshell-Enabled Photothermal Cancer Therapy: Impending Clinical Impact. *Acc. Chem. Res.* **2008**, *41*, 1842.
3. Jain, P. K.; El-Sayed, I. H.; El-Sayed, M. A. Au Nanoparticles Target Cancer. *Nano Today* **2007**, *2*, 18.
4. Han, G.; Ghosh, P.; De, M.; Rotello, V. M. Drug and Gene Delivery Using Gold Nanoparticles. *NanoBioTechnology* **2007**, *3*, 40.
5. Urban, A.; Pfeiffer, T.; Fedoruk, M.; Lutich, A.; Feldmann, J. Single Step Injection of Gold Nanoparticles through Phospholipid Membranes. *ACS Nano* **2011**, *5*, 3585–3590.
6. Eghtedari, M.; Oraevsky, A.; Copland, J.; Kotov, N.; Conjusteau, A.; Motamedi, M. High Intensity of *in Vivo* Detection of Gold Nanorods Using a Laser Optoacoustic Imaging System. *Nano Lett.* **2007**, *7*, 1914–1918.
7. Beard, P. Biomedical Photoacoustic Imaging. *Interface Focus* **2011**, *1*, 602.
8. Jin, C.; Li, Z.; Williams, R.; Lee, K.; Park, I. Localized Temperature and Chemical Reaction Control in Nanoscale Space by Nanowire Array. *Nano Lett.* **2011**, *11*, 4818–4825.
9. Nitzan, A.; Brus, L. E. Theoretical Model for Enhanced Photochemistry on Rough Surfaces. *J. Chem. Phys.* **1981**, *75*, 2205.
10. Donner, J.; Baffou, G.; McCloskey, D.; Quidant, R. Plasmon-Assisted Optofluidics. *ACS Nano* **2011**, *5*, year.
11. Challener, W. A.; Peng, C.; Itagi, A. V.; Karns, D.; Peng, W.; Peng, Y.; Yang, X. M.; Zhu, X.; Gokemeijer, N. J.; Hsia, Y.-T.; *et al.* Heat-Assisted Magnetic Recording by a Near-Field Transducer with Efficient Optical Energy Transfer. *Nat. Photon.* **2009**, *3*, 220.
12. Wang, L.; Li, B.; Thermal Memory, A Storage of Phononic Information. *Phys. Rev. Lett.* **2008**, *101*, 267203.
13. Pollock, H. M.; Hammiche, A. Micro-Thermal Analysis: Techniques and Applications. *J. Phys. D-Appl. Phys.* **2001**, *34*, R23.
14. Sadat, S.; Tan, A.; Chua, Y. J.; Reddy, P. Nanoscale Thermometry Using Point Contact Thermocouples. *Nano Lett.* **2010**, *10*, 2613–2617.
15. Löw, P.; Kim, B.; Takama, N.; Bergaud, C. High-Spatial-Resolution Surface-Temperature Mapping Using Fluorescent Thermometry. *Small* **2008**, *4*, 908.
16. Ross, D.; Gaitan, M.; Locascio, L. E. Temperature Measurement in Microfluidic Systems Using a Temperature-Dependent Fluorescent Dye. *Anal. Chem.* **2001**, *73*, 4117.
17. Baffou, G.; Kreuzer, M. P.; Kulzer, F.; Quidant, R. Temperature Mapping Near Plasmonic Nanostructures Using Fluorescence Polarization Anisotropy. *Opt. Express* **2009**, *17*, 3291.

18. Baffou, G.; Girard, C.; Quidant, R. Mapping Heat Origin in Plasmonics Structures. *Phys. Rev. Lett.* **2010**, *104*, 136805.
19. Vetrone, F.; Naccache, R.; Zamarrón, A.; Juarranz de la Fuente, A.; Sanz-Rodríguez, F.; Martinez Maestro, L.; Martín Rodriguez, E.; Jaque, D.; García Solé, J.; Capobianco, J. A. Temperature Sensing Using Fluorescent Nanothermometers. *ACS Nano* **2010**, *4*, 3254.
20. Li, S.; Zhang, K.; Yang, J. M.; Liwei, L.; Yang, H. Single Quantum Dots as Local Temperature Markers. *Nano Lett.* **2007**, *7*, 3102–3105.
21. Aiguouy, L.; Tessier, G.; Mortier, M.; Charlot, B. Scanning Thermal Imaging of Microelectronic Circuits with a Fluorescent Nanoprobe. *Appl. Phys. Lett.* **2005**, *87*, 184105.
22. Dang, N. C.; Bolme, C. A.; Moore, D. S.; McGrance, S. D. Femtosecond Stimulated Raman Scattering Picosecond Molecular Thermometry in Condensed Phases. *Phys. Rev. Lett.* **2001**, *107*, 043001.
23. Sade, S.; Nagli, L.; Katzir, A. Scanning Near Field Infrared Radiometry for Thermal Imaging of Infrared Emitters with Subwavelength Resolution. *Appl. Phys. Lett.* **2005**, *87*, 101109.
24. Van de Broek, B.; Grandjean, D.; Trekker, J.; Ye, J.; Verstreken, K.; Maes, G.; Borghs, G.; Nikitenko, S.; Lagae, L.; Bartic, C. *et al.* Temperature Determination of Resonantly Excited Plasmonic Branched Gold Nanoparticles by X-ray Absorption Spectroscopy.
25. Baffou, G.; Rigneault, H. Femtosecond-Pulsed Optical Heating of Gold Nanoparticles. *Phys. Rev. B* **2011**, *84*, 035415.
26. Boyer, D.; Tamarat, P.; Maali, A.; Lounis, B.; Orrit, M. Photothermal Imaging of Nanometer-Sized Metal Particles among Scatterers. *Science* **2002**, *297*, 1160.
27. Berciaud, S.; Cognet, L.; Blab, G. A.; Lounis, B. Photothermal Heterodyne Imaging of Individual Nonfluorescent Nanoclusters and Nanocrystals. *Phys. Rev. Lett.* **2004**, *93*, 257402.
28. Cognet, L.; Berciaud, S.; Lasne, D.; Lounis, B. Photothermal Methods for Single Nonluminescent Nano-objects. *Anal. Chem.* **2008**, *80*, 2288–2294.
29. Gaiduk, A.; Yorulmaz, M.; Ruijgrok, P. V.; Orrit, M. Room-Temperature Detection of a Single Molecule's Absorption by Photothermal Contrast. *Science* **2010**, *330*, 353–356.
30. Bon, P.; Maucort, G.; Wattellier, B.; Monneret, S. Quadriwave Lateral Shearing Interferometry for Quantitative Phase Microscopy of Living Cells. *Opt. Express* **2009**, *17*, 13080.
31. Phasics; www.phasicscorp.com; accessed January 1, 2012.
32. Thormählen, I.; Straub, J.; Grigull, U. Refractive Index of Water and its Dependence on Wavelength, Temperature and Density. *J. Phys. Chem. Ref. Data* **1985**, *14*, 933–945.
33. Tikhonov, A. N. *Solution of Ill-Posed Problems*; V. H. Winston: Washington, DC, 1977.
34. Arbouet, A.; Christofilos, D.; Del Fatti, N.; Vallée, F.; Huntzinger, J. R.; Arnaud, L.; Billaud, P.; Broyer, M. Direct Measurement of the Single-Metal-Cluster Optical Absorption. *Phys. Rev. Lett.* **2004**, *93*, 127401.
35. Celebrano, M.; Kukura, P.; Renn, A.; Sandoghdar, V. Single-Molecule Imaging by Optical Absorption. *Nat. Photon.* **2011**, *5*, 95–98.
36. Aydin, D.; Schwieder, M.; Louban, I.; Knoppe, S.; Haas, T. L.; Walczak, H.; Spatz, J. P. Micro-Nanostructured Protein Arrays: A Tool for Geometrically Controlled Ligand Presentation. *Small* **2009**, *5*, 1014–1018.

Thermal imaging of nanostructures using quantitative optical phase analysis

Guillaume Baffou,* Pierre Bon, Julien Savatier, Julien Polleux,
Min Zhu, Marine Merlin, Hervé Rigneault, and Serge Monneret
(Dated: October 19, 2011)

Supplementary information

A. Linear deconvolution numerical method

The optical index n of a material depends on the temperature T. This dependency can be approximated by a Taylor development such as:

$$n(T) = \sum_{j=0}^{M} b_j \, T^j \tag{1}$$

with T in degree Celsius and where the coefficients b_j are empirical parameters. A development at order $M = 4$ is usually sufficient to describe a condensed material over a large temperature range. For water, one has:[1]

$$\begin{aligned} b_0 &= 1.34359 \\ b_1 &= -1.0514 \times 10^{-4} \\ b_2 &= -1.5692 \times 10^{-6} \\ b_3 &= 5.7538 \times 10^{-9} \\ b_4 &= -1.2873 \times 10^{-11} \end{aligned}$$

In order to simplify the notations in the following, let us recast Eq. (1) into:

$$\delta n = \sum_{j=0}^{M} \beta_j \, \delta T^j \tag{2}$$

where

$$\delta n = n(T) - n(T_\infty), \tag{3}$$
$$\delta T = T - T_\infty \tag{4}$$

and where T_∞ is the ambient temperature. A simple calculation yields:

$$\begin{aligned} \beta_1 &= b_1 \, + \, 2\, T_\infty \, b_2 \, + \, 3\, T_\infty^2 \, b_3 \, + \, 4\, T_\infty^3 \, b_4, \\ \beta_2 &= b_2 \, + \, 3\, T_\infty \, b_3 \, + \, 6\, T_\infty^2 \, b_4, \\ \beta_3 &= b_3 \, + \, 4\, T_\infty \, b_4, \\ \beta_4 &= b_4. \end{aligned}$$

In this section, we first consider the case of sufficiently small temperature variations such that a linear dependency of the optical index as function of the temperature is a good approximation. In water, this assumption is justified as long as the temperature increase does not exceed ~ 20 K above the ambient temperature T_∞. In this case,

$$\delta n = \beta_1 \, \delta T. \tag{5}$$

As explained in the article, this thermal-induced variation of the optical index is responsible of the optical path difference (OPD) measured by the wave-front analyzer (WFA). Using the Green's formalism, the measured OPD distribution $\delta\ell_0(x, y)$ can be linked to the distribution of the heat power density (HPD) $\bar{p}(x, y)$:

$$\delta\ell_0(x, y) = [\bar{p} \otimes G_\ell](x, y). \tag{6}$$

In order to retrieve the HPD $\bar{p}(x, y)$, a deconvolution of Eq. (6) is required. This can be simply calculated in the Fourier space where a convolution becomes a simple multiplication:

$$\tilde{\bar{p}}(\mathbf{k}) = \tilde{\delta\ell}_0(\mathbf{k}) / \tilde{G}_\ell(\mathbf{k}) \tag{7}$$

where $\tilde{f}$ is the Fourier transform of f. However such a direct deconvolution is likely to cause some divergence issues when the OPD image is noisy. This mathematical problem is well-known and different solutions have been proposed. Among them, one of the simplest solution is the Tikhonov regularization technique.[2] It consists in replacing Eq. (7) by:

$$\tilde{\bar{p}}(\mathbf{k}) = \tilde{\delta\ell}_0(\mathbf{k}) \, \frac{\tilde{G_\ell}^\star(\mathbf{k})}{|\tilde{G}_\ell(\mathbf{k})|^2 \, + \, \alpha} \tag{8}$$

where $z^\star$ means the complex conjugate of z. The choice of the parameter $\alpha \neq 0$ is empirical. Figure 1 shows its effect and how it can be chosen. If α is too small, the processed OPD image is likely to be very noisy. If α is too large, it tends to damp the processed image, leading to a under-estimation of the HPD. Between these two extreme cases, a proper value of α can be chosen that tends to reduce the noise on the processed HPD without damping it. Experimentally, we found that α should not exceed 10^{-3} to ensure a proper estimation of the HPD, as seen in Fig. 1.

Once the HPD has been calculated using the Tikhonov method, we simply work out the temperature distribution, still in the Fourier domain, using the Green's function G_T:

$$\tilde{\delta T}(\mathbf{k}) = \tilde{\bar{p}}(\mathbf{k}) \, \tilde{G_T}(\mathbf{k}) \tag{9}$$

followed by an inverse Fourier transform of $\tilde{\delta T}(\mathbf{k})$. Figure 2 summarizes the overall procedure using a block diagram.

B. Non-linear algorithm

In the most general case, *i.e.* when the temperature increase exceeds ~ 20 K (in water), the non-linear (NL)

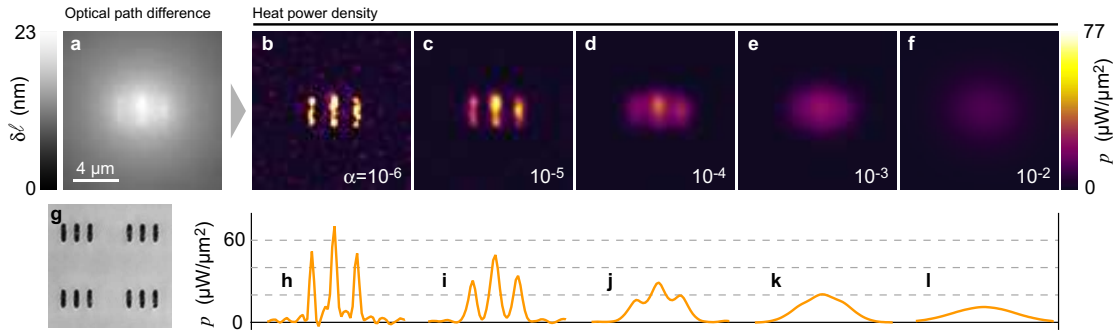

FIG. 1. Influence of the choice of the Tikhonov parameter α illustrated on a gold microstructure featuring 3 rectangle areas composed of arrays of quasi-hexagonally organized gold nanodots. The structure was illuminated at $\lambda = 532$ nm and $I = 216$ µW/µm^2. a) Thermo-induced optical path difference on a microstructure composed of 3 parallel rectangle areas of gold nanoparticles. b-f) Heat power density distributions computed using different Tikhonov parameters α. g) Optical image of the structures. h-l) Associated HSD profiles average over 16 horizontal lines.

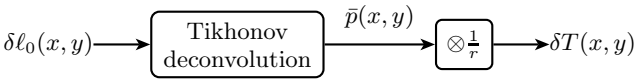

FIG. 2. Block diagram describing the numerical procedure used to work out the HPD $p(x, y)$ and temperature $T(x, y)$ distributions from the measured OPD distribution $\delta\ell_0(x, y)$.

dependence of the optical index as function of the temperature cannot be discarded. This would rapidly yield an over-estimation of the temperature increase. The Taylor development at least at the fourth order becomes a requirement:

$$\delta n = \beta_1 \delta T + \beta_2 \delta T^2 + \beta_3 \delta T^3 + \beta_4 \delta T^4 \qquad (10)$$

To illustrate the influence of the NL terms, δn has been plotted as a function of T for Taylor developments at the 1$^{\text{st}}$, 2$^{\text{nd}}$, 3$^{\text{rd}}$ and 4$^{\text{th}}$ orders in Fig. 3.

Let us first consider the case of a point-like source of heat $\bar{p}(x, y) = \bar{P}_0 \delta(x)\delta(y)$. Eq. 9 of the article derived when $n(T)$ was linear is no longer valid in the present case. Using Eq. (10) and $\delta T(\rho, z) = \bar{P}_0/\sqrt{\rho^2 + z^2}$, the calculation of the integral $\delta\ell(\rho) = \int_0^h \delta n(\rho, z)\mathrm{d}z$ yields an analytical solution:

$$\begin{aligned}\delta\ell(\rho) = {} & \bar{P}_0\, \beta_1\, \ln(u + \bar{u}) \\ & + \bar{P}_0^2\, \beta_2\, \frac{1}{\rho}\, \tan^{-1}(u) \\ & + \bar{P}_0^3\, \beta_3\, \frac{1}{\rho^2}\, \frac{u}{\bar{u}} \\ & + \bar{P}_0^4\, \beta_4\, \frac{1}{\rho^3}\, \frac{1}{2}\, \left[\frac{u}{\bar{u}^2} + \tan^{-1}(u)\right] \end{aligned} \qquad (11)$$

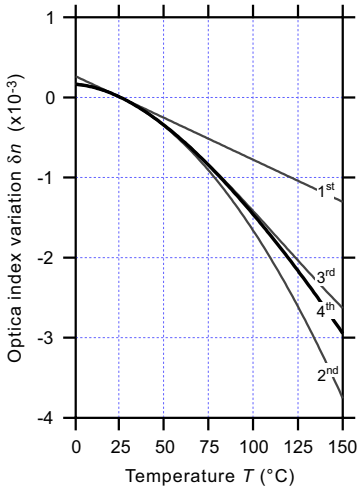

FIG. 3. Variation of the optical index of water $\delta n = n(T) - n(25°)$ as function of the temperature. Taylor developments at the 1$^{\text{st}}$, 2$^{\text{nd}}$, 3$^{\text{rd}}$and 4$^{\text{th}}$orders are plotted according to Eq. (10).

where

$$u = h/\rho$$
$$\bar{u} = \sqrt{1 + u^2}.$$

Eq. (11) can be used to accurately retrieve the heat power $\bar{P}_0$ from the temperature profile generated by the localized source of heat, independently on the temperature range.

Interestingly,

$$\begin{aligned} \ln(u+\bar{u}) &\underset{h\to\infty}{\sim} -\ln(\rho) \\ \tan^{-1}(u) &\underset{h\to\infty}{\longrightarrow} \pi/2 \\ u/\bar{u} &\underset{h\to\infty}{\longrightarrow} 1 \\ u/\bar{u}^2+\tan^{-1}(u) &\underset{h\to\infty}{\longrightarrow} \pi/4. \end{aligned}$$

Consequently, when the surrounding liquid layer can be considered as infinitely thick (compared to the extension of the temperature distribution), one ends up with a simpler formula:

$$\delta\ell(\rho) = -\bar{P}_0\,\beta_1\,\ln(\rho) + \frac{\pi\,\bar{P}_0^2\,\beta_2}{2\,\rho} + \frac{\bar{P}_0^3\,\beta_3}{\rho^2} + \frac{\pi\,\bar{P}_0^4\,\beta_4}{4\,\rho^3}$$

Let us consider now a *non-localized* source of heat $\bar{p}(x,y)$. Unfortunately, the simple procedure introduced in the previous section – based on the Green's formalism and the Tikhonov deconvolution algorithm – is no longer valid if non-linearities occur. To overcome this problem, several deconvolution techniques can be used. We proposed here to use a procedure that relies on an iterative algorithm where the HPD $\bar{p}(x,y)$ is refined at each loop i. The procedure is schematized in Fig. 4.

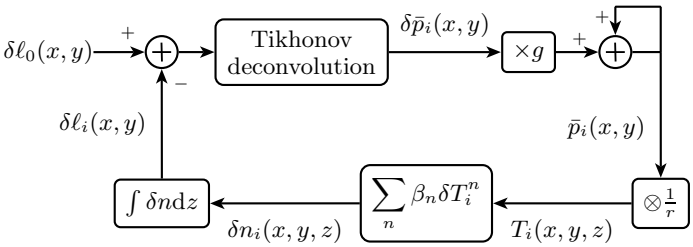

FIG. 4. Block diagram describing the numerical procedure used to work out the HPD $p(x,y)$ and temperature $T(x,y)$ distributions from the measured OPD distribution $\delta\ell_0(x,y)$.

In the first loop ($i=1$), a HPD $\bar{p}_1(x,y)$ is computed from the measured OPD using the linear Tikhonov algorithm. This first estimation of the HPD is then convoluted in 3 dimensions (3D) by the Green's function $G_T(\mathbf{r})$ over the whole liquid layer, which leads to a first estimate of the temperature distribution in 3D $T_1(x,y,z)$ within the whole liquid layer. Then, a first estimate of the 3D profile of the optical index $\delta n_1(x,y,z)$ is calculated from the temperature profile using its NL expression (Eq. (10)). Finally, by integrating the OPD over the z direction, one ends up with an OPD map $\delta\ell_1(x,y)$. In the linear case, one should get $\delta\ell_1(x,y) \approx \delta\ell_0(x,y)$ (if the damping factor $g=1$) but the non-linearities generate a discrepancy. For this reason, at each loop, the difference $\delta\ell_0 - \delta\ell_{i-1}$ is re-injected into the numerical procedure to compute a HPD correction $\delta\bar{p}_i$. Then, the corrected HPD $p_{i-1}+\delta p_i$ is used to compute a new OPD map $\delta\ell_i$. This procedure can be iterated as many times as desired to get a distribution $\bar{p}(x,y) = g\sum_{i=1}^{N}\delta\bar{p}_i(x,y)$ that generates a OPD distribution $\delta\ell_N$ as close as possible to the measured OPD $\delta\ell_0$. Note that a damping factor g ($0 < g \leq 1$) can be introduced in the procedure. It makes the evolution toward the proper OPD distribution $\delta\ell_0$ slower but more accurate and it ensures convergence. $g \approx 0.3$ is usually a good compromise.

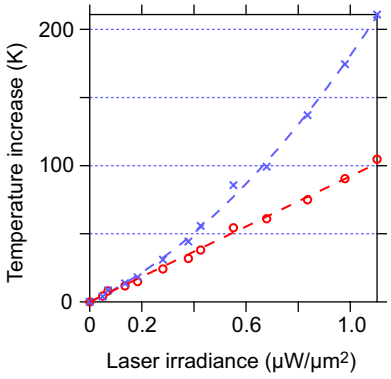

FIG. 5. Average temperature increase of a plus-shape structure as function of the laser irradiance. Blue crosses (×): Artefactual curve obtained when not using the NL algorithm, leading to an overestimation of the temperature. Red circles (○): Proper and expected linear dependance of the temperature increase as function of the laser irradiance obtained when using the NL algorithm, supporting his validity.

In order to illustrate the effect of this NL approach compared to the linear approximation, Fig. 5 plots the evolution of the temperature measured on a given structure as function of the laser power using the linear and NL algorithms. One can see that above a temperature increase of 20 K, it becomes necessary to use the non-linear algorithm. Note that when using the NL algorithm, one does observe a linear variation of the temperature as function of the laser power, which is the expected behavior.

Using this iterative algorithm is the choice we have done for the sake of simplicity. However, it could be interesting in the future to investigate other possible optimization techniques based on the minimization of an approximation criterion such that $\iint \left[\delta\ell_0(x,y) - \int_0^h \delta n \mathrm{d}x\mathrm{d}y\right]^2$.

C. Principle of wavefront analysis using quadri-wave lateral shearing interferometry

The thermal measurements presented in the article are based on quadriwave lateral shearing interferometry (QWLSI) measurements. In this section, we wish to give a brief description of the principle of this technique. For more details, we invite the reader to refer to Refs. [3],[4]

and [5].

One-dimensional lateral shearing interferometry is a technique aiming at measuring the phase gradient of a given light wavefront in one direction from the interference between two identical but tilted copies of the wavefront. Such an approach does not require the use of any reference light beam, which is a crucial advantage. The replication of the incident wavefront is achieved using a sinusoidal phase grating (Fig. 6). After a few millimeters of propagation, the mutual interference pattern is recorded with a CCD camera. In the simplest case of a flat incident wavefront, the interference pattern consists of regular fringes featuring a period Λ (Fig. 6a), leading to two well-defined spots in the Fourier space at the spatial frequencies $\pm 1/\Lambda$ (Fig. 6b). In the case of an arbitrarily distorted wavefront, a local phase gradient leads to a local variation of the fringe frequency. In practice, phase gradients are recovered in the Fourier space by means of a deconvolution around the nominal interferogram fringe frequency $1/\Lambda$ (Fig. 6d).

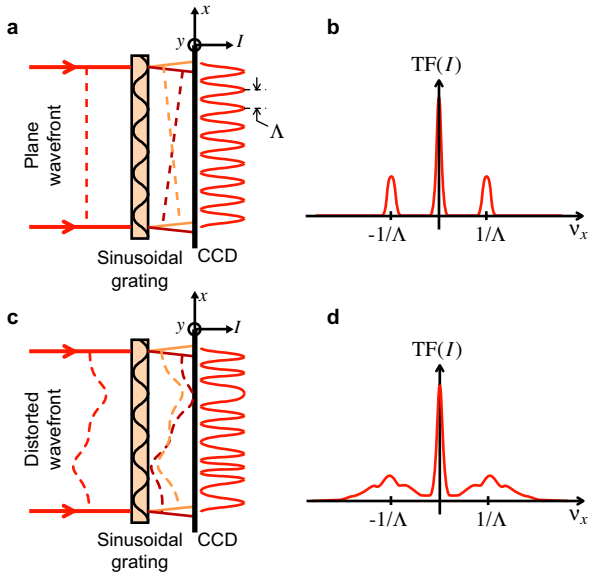

FIG. 6. Principle of QWLSI. (a) Formation of regular fringes of period Λ generated by a flat wavefront duplicated by a sinusoidal phase grating. (b) Fourier-transform of the resulting interferogram in the spatial frequency domain. (c) and (d): same as (a) and (b) in the case of arbitrary wavefront.

In order to obtain two-dimensional (2D) images, a 2D phase grating has to be used (Fig. 7). Such an approach, called quadriwave lateral shearing interferometry (QWLSI),[3] leads to four replicas of the incident wavefront that interfere all together. The interferogram is recorded by a CCD. The two processed gradient profiles along two crossed directions are then integrated to determine both the intensity and the phase of the incident field by deconvolution around the frequency $1/\Lambda$.[4] As for one-dimensional lateral shearing interferometry, one could use a sinusoidal two-dimensional phase grating to generate the 4 replicated wavefronts required by QWLSI (Fig. 7a). In practice, the so-called Modified Hartmann Grating (MHG) is preferably used because of its much simpler fabrication process: MHG, as shown in Fig. 7b, is an only 3-level amplitude component that has been optimized by properly choosing the ratio between the size of the square holes and the pitch of the grating[5] to diffract more than 90% of the light energy into the 4 first orders required in QWLSI.

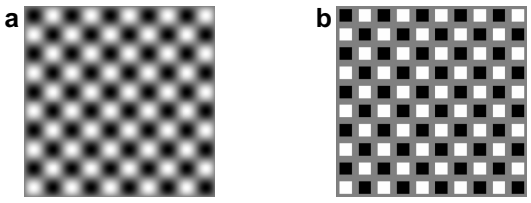

FIG. 7. Transmission map of the two-dimensional diffractive component required for QWLSI. (a) Nominal sinusoidal phase grating that would give perfect QWLSI. (b) Simplified 3-level component, known as the "modified Hartmann grating", made of a combination of an amplitude grating with a π-shift phase chessboard grating.

The intensity distribution on the CCD sensor can be calculated from the coherent addition of the four displaced replicas. Assuming a paraxial propagation and neglecting free space diffraction, the intensity distribution reads:[6]

$$I(\mathbf{r},z) = I_0\left\{1+\left[\cos\left(\frac{2\pi}{\Lambda}x+\frac{2\pi}{\Lambda}z\frac{\partial\delta\ell}{\partial x}\right)+\cos\left(\frac{2\pi}{\Lambda}y+\frac{2\pi}{\Lambda}z\frac{\partial\delta\ell}{\partial y}\right)\right]\right.$$
$$\left.+\frac{1}{2}\left[\cos\left(\frac{2\pi}{\Lambda}(x+y)+\frac{2\pi}{\Lambda}z\frac{\partial\delta\ell}{\partial(x+y)}\right)+\cos\left(\frac{2\pi}{\Lambda}(x-y)+\frac{2\pi}{\Lambda}z\frac{\partial\delta\ell}{\partial(x-y)}\right)\right]\right\}$$

where z is the propagation length along the optical axis, and I_0 is the maximum intensity of the incident light at

the entrance of the MHG ($z = 0$). This equation shows that both the interferogram period and the modulation due to the OPD are wavelength-independent. The use of a temporally incoherent broad-band source (as a halogen lamp) is thus possible.[5,6] As described in the paper, we directly benefited from such an achromatic property by simply using the native broadband halogen source of the system to measure thermo-induced refractive index changes in the sample.

Because phase information is coded in the interferogram by a spatial frequency modulation, phase and intensity of the incident light beam are independently determined. The price for this is that the resulting phase image is 4 times smaller in lateral size than the original interferogram image recorder onto the CCD. Indeed, 4×4 pixels of the CDD are used to process one pixel of the phase image. However, the advantage is that this CCD-based approach provides single-shot quantitative phase imaging and thus high speed and high resolution measurements.

---

* guillaume.baffou@fresnel.fr

[1] I. Thormählen, J. Straub, and U. Grigull, J. Phys. Chem. Ref. Data **14**, 933 (1985).

[2] A. N. Tikhonov, *Solution of Ill-posed problems* (Vh Winston, 1977).

[3] J. Primot and L. Sogno, J. Opt. Soc. Am. A **12**, 2679 (1995).

[4] S. Velghe, J. Primot, N. Guérineau, M. Cohen, and B. Wattellier, Opt. Lett. **30**, 245 (2005).

[5] J. Primot and N. Guérineau, Appl. Opt. **39**, 5715 (2000).

[6] P. Bon, G. Maucort, B. Wattellier, and S. Monneret, Opt. Express **17**, 13080 (2009).